Numerical Modeling and Analysis of a Hydrokinetic Turbine in a Confined Geometry

Jaikeun Chung

The Ohio State University

Undergraduate Honors Thesis

2019

Abstract

As a renewable and reliable source of energy, hydropower provides around 17% of the electricity production in United States. Hydropower takes on many forms and the most common method of them is using a potential energy through a dam which typically involves large construction costs. Compared to this conventional form of hydro power generation, the use of hydrokinetic power doesn't require large civil engineering works since hydrokinetic turbines can be installed with no or small modifications to existing infrastructure, but they are not yet widely employed due to operating in lower energy density resource. Research of utilizing hydrokinetic energy are mainly focused on large applications such as a tidal power, rather than small scale river applications such as discussed in this study. While the power output of a small hydrokinetic turbine for river or canal application will typically be in the micro or pico-power range, there is a case to be made for the installation of such devices when designed cost efficiently.

The main objective of this research is the development of a three-dimensional Computational Fluid Dynamic (CFD) model of a hydrokinetic turbine by using Finite Volume Method (FVM). Ansys FLUENT19.1 was employed in order to analyze the Smart Free-Stream turbine designed by Smart Hydro Power GmbH in a canal setting. The flow field as well as the power output of the turbine were analyzed for various water velocities and rotational speeds. The results were then compared to measured values provided by the turbine manufacturer. The goal is to be able to provide accurate power predictions from CFD modeling to evaluate the cost and efficiency of more complex scenarios (i.e. Multiple turbines in complex canal geometries) in advance to committing to such installation projects.

Acknowledgement

I would like to thank Dr. Clarissa Belloni for having kindly directed me during the research period as a primary advisor. It was great lucky that I conducted this research with her since she had cared her students with a lot of attention while encouraging them to have a professionalism. Conducting this study was also great opportunities to learn not only relative knowledges but also overall understandings of the research project.

I also would like to thank Dr. Sandip Mazumder for guidance of the project. Comprehensive understanding of the CFD was possible with his suggestions and detailed reviews. Especially, I appreciate that he gladly accepted the examiner of this research and gave me lots of feedbacks.

I want to give special thanks to Zhenyu Wang. He had showed me lots of technical methods of utilizing CFD and OSC system often when I stuck. Also, he gave me many guidance to build proper modeling for this study. The research would take much more time without his helps.

I thank Smart Hydro Power, GmbH for providing geometry of the turbine and data used in this research, and staffs of SIM Center for coordinating laboratory and internship during the summer.

Lastly, I thank the Ohio Supercomputer Center for allowing to use computing resources from them. It was very helpful to reduce time for calculations and I think it was almost impossible to conducting this research in time without using it.

Table of Contents

Table of figures

Nomenclature

Latin Symbols

A	area
a	acceleration
B	blockage ratio
b	source matrix
C_p	power coefficient
D_h	hydraulic diameter
E	total energy
F	force
f_b	body force
H	head
I	turbulent intensity
k	turbulent kinetic energy
l	length
$\dot{m}$	mass flow rate
P	power
p	pressure
q	heat flux
Re	Reynolds number
S	surface vector
T	torque
TS	Stress tensor
t	time
u	flow velocity
V	volume
Y+	near wall function (y-plus)

Greek Symbols

∇	del operator
Γ	diffusion coefficient
μ	dynamic viscosity
μ_t	eddy viscosity
ε	dissipation rate of kinetic energy
λ	tip speed ratio
ω	specific dissipation rate
ω	angular velocity
ν	kinematic viscosity

Chapter 1 Introduction

Current methods of employing hydropower and the advantages of small-scale applications of hydrokinetic energy are introduced in section 1.1. Following section introduces a turbine used in this study and explains significance of the research through relevant studies. The purpose of the thesis is summarized in section 1.3 and overview of following chapters are briefly described in section 1.4.

1.1 Hydrokinetic Energy versus Traditional Hydropower

Hydropower is one of the leading sources of renewable energy, and it exploits the natural circulation of water - evaporation and precipitation. Typically, hydropower is extracted as a potential energy, by the means of a dam construction to achieve a large head height. The dam construction comes at a high environmental cost as well as a very large monetary investment due to the extensive civil engineering works. A dam is built with multiple purposes in mind, typically electricity production, flood control, as well as water supply. Some plants also act as a type of battery by using pumps to transfer the water back into the reservoir during low electricity demand. Turbines like a Pelton and Francis, widely used in dam hydropower plants require a certain level of water, head, H for stable generation which entails a reservoir. The head of the reservoir is also controlled based on the climate conditions and water usage when the reservoir acts as a main water supply. Reservoirs require a large footprint to contain the water. In order to

create a reservoir a dam usually blocks a natural stream and even though eco-friendly designs are introduced (i.e. spillway for migratory fish, fish ladders) destroying habitats of endangered species or domestic flora is inevitable and deposition of sediments or decrease of stream velocity may cause many other environmental issues.

Figure 1. 1. Hydrokinetic turbine (Hydro Green Energy) in Mississippi River

Instead of the using the potential energy in an artificial way, employing natural currents or stream can have advantages over the problems described above. A hydrokinetic turbine (Figure 1.1) has similar structure to a wind turbine, with its blades rotating due to the kinetic energy contained in the fluid, in this case water. This type of turbine does not need a head of water, though the water depth should be sufficient to submerge overall turbine structure. The generated power from a kinetic turbine is directly related to its size and the velocity of the current, which described in later section 4.4. Thus, the power output fluctuates according to the

fluctuations in the natural conditions, such as the discharge of the stream or velocity of ocean current. A larger size of turbine rotor is also preferred when it is necessary to yield more power, though blade loading, and vibrations can lead to engineering challenges with higher investment costs.

1.2 Significance

Among many ongoing research studies on hydrokinetic energy, using a current of ocean or tidal energy is one of the most actively studied, but has yielded only few installed applications so far. Offshore construction for tidal power is often challenging and expensive due to corrosion by salinity, muddy seabed and varying sea level and conditions. Often large distance between possible energy consuming regions (i.e. residential area) and the tidal energy farm can cause further issues, as it may necessary to build additional infrastructure and losses of energy are inevitable. However, tidal and marine currents are still considered to have high energy potential, for example, Stegman and her team (2017) estimated the available energy from tidal stream in UK is approximately 20 to 30 TWh/year and a research from Electronic engineering department of National university of Ireland (2013) assumed 2.476 MW of energy can be generated through employing 254 tidal devices. Several forms of turbine devices are developed for extracting energy from the tide, but the axial turbine devices are currently showing the most promising outcomes, and prototypes of them have been tested in the field (Belloni, 2013).

Micro hydropower plants, typically defined as producing less than 100 kW (Gosh, 2011) by adopting axial-flow hydrokinetic turbines, may yield several advantages compared to either above discussed tidal applications. For one it can be installed near the consumer and tied directly

into the existing grid. Secondly, such an installation can make use of existing civil infrastructure, such as bridges or canals, and accessibility is much less of an issue.

One example of a hydrokinetic turbine is the Smart Hydro Power Free-Stream turbine (Figure 1.2) which has been designed for application in canals which will form the subject of this study.

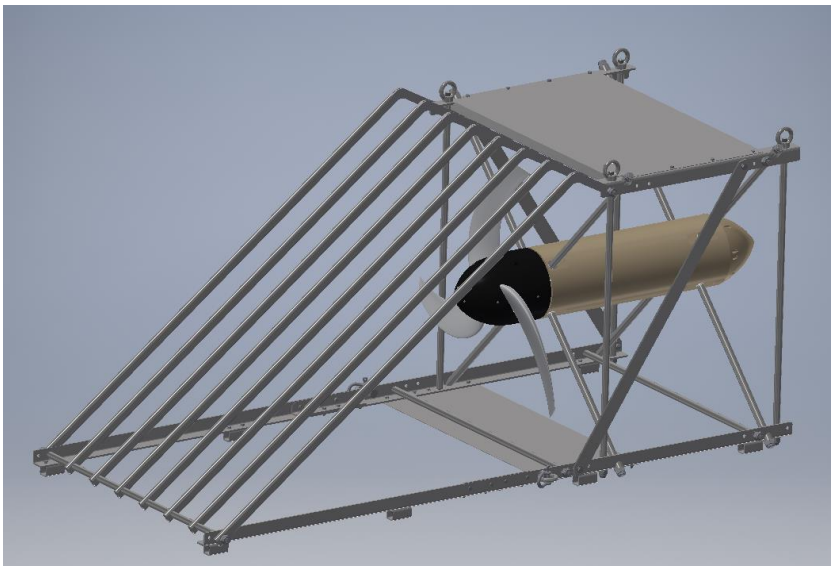

Figure 1. 2. Smart Free Stream turbine, designed by Smart Hydro Power, GmbH

The Free Stream turbine consists of three main parts, rotor (blades part in this analysis), debris protector and underwater generator with 5kW of maximum capacity. Specifics of the turbine are shown in table 1.1,

Table 1.1. Technical Specifics of Smart Hydro Turbine

Energy Yield (W)	250-5000
Height (m)	1.12
Width (m)	1.12

Length (m)	2.64
Weight (kg)	300

The minimum geometrical requirements for channel to install the turbine is slightly bigger than its size, therefore numerous canals can be considered as a potential installation place. Installations of a group of turbines side by side is an option to increase power output from a given canal.

A canal is an artificial channel designed to guide water along an intended path, other than a natural river. Canals are traditionally used for transport, irrigation and drainage. Set up the canal geometry as a flow domain in Computational Fluid Dynamics (CFD) analysis may different from previous relevant studies since a flow boundary generally assumed as empty field while canal has a specified geometry. A shape of flow domain is pre-determined by existing canals, instead of reasonably selected with CFD techniques. Another difference with previous researches may come from existence of the turbine frames, debris protector. The Free Stream Turbine contains a protector to prevent damages on rotor by buoyant objects (i.e. wastes or gravel). Filtering these out helps to increase life span, but effect from the protector should be considered since it may cause disturbance of the flow and eventually decrease power outputs.

In a study of river hydrokinetic turbine optimization (Muratoglu, et al. 2017), overall turbine propeller structure (TIGRIS-27) was tested with different types of hydrofoil to find an ideal design among them. The flow regime boundary used in this study was set as a far-field wall to avoid interference - viscous effect from there. Similar flow domain is used when CFD studies about hydrokinetic turbine includes structures other than a bare blade, such as ducted (Belloni,

2013) or diffuser-augmented (Tampier et al. 2017) types. In these studies, effect of duct and diffuser were investigated with a propeller as displayed in Figure 1.3

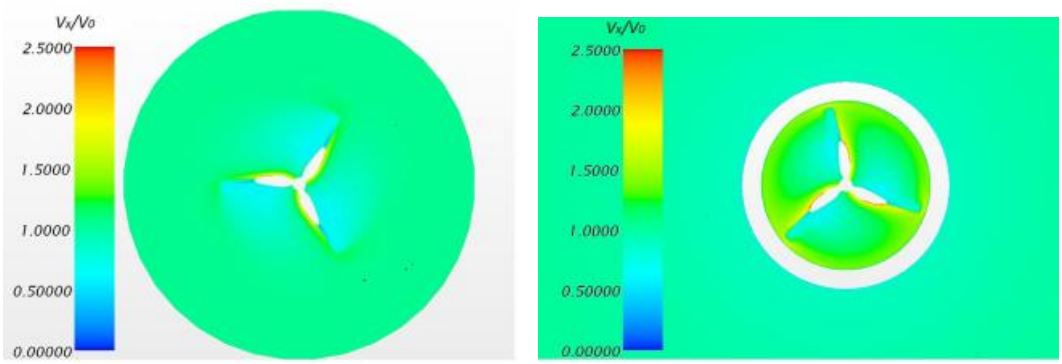

(a) Bare propeller analysis (b) Augmented turbine analysis

Figure 1. 3. CFD analysis of hydrokinetic turbine with (b) and without (a) a diffuser conducted by Tampier and his team in Universidad Austral de Chile

Duct and diffuser were set to have shear drag, but outer surfaces of the flow domain which employed in these studies were assumed as slip wall or having symmetry condition to eliminate effect from the domain itself. A hydrokinetic turbine with more complex structure was numerically tested by Riglin et al (2016). In this study, a prototype of river applicable hydrokinetic turbine was examined, which have a duct, six cylindrical supporters. However, in the numerical test, the cylindrical domain was employed while extended to 20 times of blade diameter instead of a river geometry.

1.3 Purpose of proposed research

The objective of this research is on figuring out a performance of the hydrokinetic turbine though CFD modeling. While the Free-Stream turbine introduced in section 1.1 has been employed in the field in multiple locations, no study has been performed to model the turbine in various canal geometries. This thesis will provide a simulation foundation that can be used to study the turbine in a multitude of configurations.

1.4 Thesis Overview

Following chapters discuss about the research specifics

Chapter 2

The mathematical baselines employed for turbulent model and Finite Volume Method (FVM) method in Ansys Fluent are described in this chapter. The chapter examine how non-linear properties of fluid would calculate with empirical relationships and discretization would be applied to fluid equations.

Chapter 3

The chapter explains basic flow characteristics of the open channel flow, and how boundaries were set in the modeling. Specifics of mesh generation and grid study are follows.

Chapter 4

Simulation results are discussed in this chapter. Torque and power outcomes from the modeling are compared with different physical setups while interpret fluid behavior in the flow filed.

Chapter 5

In addition to conclusions from simulation results, shortcomings of the research and possible future works, came from limited research time and software access are described in the last chapter.

Chapter 2 CFD and RANS Modeling

Many fluid and energy equations may be branched out from few numbers of equations, but it is important to reduce variables or complexity to get faster and more accurate results. Solver programs could employ same baseline governing equations for fluid or energy flows which decided by a user, but different algorithms or methods could be adopted to solve them. Many non-dimensional parameters have an importance since it makes to assume fluid behaviors beforehand and reduce scope of equations or what equations have the most significance. Mathematical and theoretical bases of fluid dynamics which used in this research are briefly introduced in section 2.1 while its adoptions for CFD and turbulent modeling are explained in following sections, 2.2 and 2.3. Following sections of 2.4 and 2.5 explain a discretization process through Finite Volume Method (FVM) and linearization algorithm employed by Fluent 19.1.

2.1 Governing Equations

When an object is subjected to external force, it reacts very differently according to their physical conditions, such as solid and fluid. Fluids exhibits very small resistance against tangential shear force; therefore, they continuously deform over time when force is applied. Therefore, a continuum assumption with Eulerian approach (space and time) is generally used in fluid mechanics and CFD instead of a Lagrangian method which tracking individual particles.

Three different conservation laws: mass, momentum and energy consist governing equations of flow analysis (Kajishima, and Taira, 2017). In a special condition – Newtonian fluid, the set of equations are called Navier-Stokes equations and it is necessary reduce variables from them according to flow conditions used in this research.

A mass fluxes in and out through an arbitrary control volume should be zero (mass conservation), and its expression in the differential form is

$$\frac{\partial \rho}{\partial t} + \nabla \cdot (\rho u) = 0 \qquad (2.1)$$

where ρ = density, t = time ∇ = Del operator and u= flow velocity

Force and momentum relationship can be expressed with the Newton's seconds law (F=ma) and the motion of the flow can be presumed by a force balance. Conservation of momentum of the fluid flow is

$$\frac{\partial(\rho u)}{\partial t} + \nabla \cdot (\rho u u - TS) = \rho f \qquad (2.2)$$

where TS = Stress tensor and f = body force acting on the fluid

From the Newton's second law, a force is expressed to have two components: body with a gravity and surface with a pressure and viscous terms. Stress tensor is dependent on fluid characteristics and applied pressure, and it becomes proportional to the viscosity when subjected material is a Newtonian fluid. The equation of motion (eq. 2.2) have five unknown variables: density, velocity, pressure, shear and body forces but these are further reduced when the density of fluid is constant (incompressible),

$$\left[\frac{\partial u}{\partial t} + \nabla \cdot (uu)\right] = -\nabla p + \nabla \cdot (2\mu D) + \rho f \qquad (2.3)$$

where μ = dynamic viscosity, p=pressure and D = rate of strain tensor

Conservation of energy (eq 2.4) can be used for determining material properties such as density and viscosity from empirical equations. Depends on fluid solver program, the energy conservation can be applied to momentum and mass conservations either simultaneously or afterwards, but it adds another complexity on the calculations, therefore it is usually applied when a fluid is compressible, or effect of heat transfer and temperature change is considerable.

$$\rho \frac{\partial E}{\partial t} + \nabla \cdot (\rho \mathrm{Eu} - \mathrm{TS} \cdot \mathrm{u} + \mathrm{q}) = \rho u \cdot f \qquad (2.4)$$

where E = total energy and q = heat flux

Energy conservation was not considered in this research since the flux of thermal energy was not anticipated. Therefore, the Navier-Stokes equations for incompressible turbulent flow can be expressed in the Cartesian coordinate system as below,

$$\frac{\partial u_i}{\partial t} + \frac{\partial (u_i u_j)}{\partial x_j} = -\frac{1}{\rho}\frac{\partial p}{\partial x_i} + \frac{\partial}{\partial x_j}(2\nu D_{ij}) \qquad (2.5)$$

where u_i = velocity components in x-dir., u_j = velocity components in y-dir., x_i = spatial dimension in x-dir., x_j = spatial dimension in y-dir. and ν = kinematic viscosity (ν=μ/ρ)

The non-linearity of this equation, originated from shear strain of the flow, denoted as D_{ij} makes it to very difficult to solve and the linearization processes are explained in following sections.

2.2 Reynolds Averaged Navier Stokes (RANS) Equations

Fluid shows different phases of flow according to the material properties and physical conditions: laminar and turbulent. Analytical approaches to them should be different since a

laminar flow have consistent streamlines while eddies and vortices, induced by natural convection in turbulent regime are highly unpredictable and chaotic. Non-dimensional quantities are used to determine various flow characteristics and the Reynolds number (eq. 2.6), as one of them, indicates whether the flow is located in laminar or turbulent regions through measuring inertial and viscous force balance (Belloni, 2013),

$$Re = \frac{\rho u D_h}{\mu} \tag{2.6}$$

where D_h = Hydraulic diameter

Both flows can be expressed with N-S equation but only few cases have analytic solutions since the partial differential equation is non-linear even though it is further reduced assumptions with no-body force, steady state and laminar flow. Non-dimensionalization technique (eq 2.7) is used to solve problems with laminar flow field while making a variable only as the Reynolds number (Kajishima, and Taira, 2017).

$$\frac{\partial u_i^*}{\partial t} + u_j^* \frac{\partial u_i^*}{\partial x_j^*} = -\frac{1}{\rho}\frac{\partial p'^*}{\partial x_i} + \frac{1}{Re}\left(\frac{\partial^2 u_i^*}{\partial x_j^* \partial x_j^*}\right) \tag{2.7}$$

where superscripts (*) represent the non-dimensional quantity of the components

In turbulent regime, the flow is intrinsically unsteady, and its exact solution might achievable with Direct Numerical Simulation (DNS) method, which solves all of the effective eddies by using extremely fine grids. It costs lots of computing resources, therefore generally applicable to very simple geometries with modern computing power.

Reynolds Averaged Navier-Stokes (RANS) equation suggests empirical approach to solve turbulent problems with averaging fluctuations with a turbulence closure which decides turbulent

shear stress term. In the RANS equation, the instantaneous velocity from the flow is treated as to have two different velocity components: mean velocity and fluctuation.

$$u = \bar{u} + u' \tag{2.8}$$

where $\bar{u}$ = averaged velocity and u′= fluctuation

Applying the velocity components with the assumption of incompressible flow to the continuity (eq. 2.1) and momentum conservation (eq. 2.2) results equations of 3.9 and 3.10.

$$\frac{\partial \overline{u_k}}{\partial u} = 0 \tag{2.9}$$

$$\frac{\partial \bar{u}_i}{\partial t} + \frac{\partial (\bar{u}_i \bar{u}_j)}{\partial x_j} = -\frac{1}{\rho}\frac{\partial \bar{p}}{\partial x_i} + \frac{\partial}{\partial x_j} + \frac{\partial}{\partial x_j}(-\tau_{ij} + 2\nu \bar{D}_{ij}) \tag{2.10}$$

where $\overline{u_k}$ = averaged velocity components in z-dir. τ_{ij}= Reynolds stress

Reynold's stress tensor ($\rho\tau_{ij}$) is added separately to laminar flow and it later decided by a type of closures.

$$\tau_{ij} = \overline{u_i' u_j'} \tag{2.11}$$

where $\overline{u_i'}$ = mean fluctuation in x-dir. and $\overline{u_j'}$= mean fluctuation in y-dir.

The stress tensor for turbulent flow have 6 variables which makes total ten unknowns with mean velocities for x, y and z directions and the mean pressure. Depend on the required accuracy or modeling specifics, different number of transport equations are employed to decide quantity of turbulence.

2.3 Turbulent Modeling

Even though most terms of RANS equation are linearized (eq. 2.9), analytical solution is still not possible due to non-linear stress tensor (eq. 2.10). Using different types of closer determines shear terms. As discussed in section 1.2, k-ω SST (Shear Stress Transform) is frequently adopted as turbulent closer for flow separation problems, and show more accurate results with various flows, for example, adverse pressure gradient flows or airfoil (Ansys Fluent Guidebook).

The separated Reynold's stress tensor by RANS approach is linearized based on the Boussinesq hypothesis (Moukalled et at., 2016), which assume the shear stress is a linear function of time-mean velocity in Newtonian fluid. With this assumption, the stress tensor ($\tau^R = \rho\tau_{ij}$) for incompressible flow is expressed as,

$$\tau^R = -\rho\overline{u'u'} = \mu_t\{\nabla \mathrm{u} + (\nabla u)^T\} - \frac{2}{3}\rho k I \qquad (2.12)$$

where I= turbulent intensity, k=turbulent kinetic energy and μ_t = eddy viscosity

Turbulent kinetic energy (k) and turbulent eddy viscosity (μ_t) terms are adopted for quantify turbulence and the fluid equations become quasi-steady states. The kinetic energy is defined in Equation 2.13, but the viscosity term is decided while employing different number of transport equations.

$$\mathrm{k} = \frac{1}{2}\overline{u' \cdot u'} \qquad (2.13)$$

Two equation models: k-ε and k-ω are most frequently used in practical analysis and the difference between them came from converting turbulence kinetic energy into rate of dissipation (ε) or into internal thermal energy (ω). From these, the Baseline k- ω model and Shear Stress

transport (SST) model were developed to supplement weakness of previous two models. By combining the k-ε into k-ω model overall accuracy of the turbulent modeling is increase since a boundary layer edge and near wall surface which each model has better precisions were combined.

2.4 Finite Volume Method (FVM)

Fluid and heat flux can be expressed in a differential form. In FVM, a discretization refers to make the overall domain divided into much smaller cells which has individual control volumes. Cells are assumed to have certain physical quantities in its centers, such as temperature and velocity, and substitutes variables of the linearized differential equations through mathematical approximations, for example, Taylor Series expansion.

The conservation equation of heat and fluid flux (eq. 2.14) have following scalar form in general (Moukalled et al., 2016),

$$\frac{\partial(\rho\Phi)}{\partial t} + \nabla \cdot (\rho u \Phi) = \nabla \cdot (\Gamma^{\Phi} \nabla \Phi) + Q^{\Phi} \tag{2.14}$$

where Γ=diffusion coefficient

The equation has four terms in following orders: Transient, convective, diffusion and source. Each control volumes have discretized equation (eq. 2.15) with steady-state assumption. The Gaussian theorem is applied to express convection and diffusion terms in surface integrals

$$\oint_{\partial V_c} (\rho u \Phi) \cdot dS = \oint_{\partial V_c} \Gamma^{\Phi} \nabla \Phi \cdot dS + \oint_{V_c} Q^{\Phi} dV \tag{2.15}$$

where S = surface vector and V = Volume

In the incompressible flow, the RANS equation and turbulent tensor are converted into a matrix form and iterative methods are used solve algebraic equations since an explicit method or direct method for solving the momentum equation is unavailable (Moukalled et al., 2016).

Discretization of continuity and momentum equations (eq 2.1 and 2.2) with a steady state assumption are yielded as

$$\int_{V_c} \frac{\partial(\rho u)}{\partial x} dV = 0 \tag{2.16}$$

$$\int_{V_c} \frac{\partial uu}{\partial x} dV = \int_{V_c} \frac{\partial}{\partial x}\left(\mu \frac{\partial u}{\partial x}\right) dV - \int_{V_c} \frac{\partial P}{\partial x} dV \tag{2.17}$$

A one-dimensional volumetric flow filed can be expressed as following diagram (Figure. 2.1)

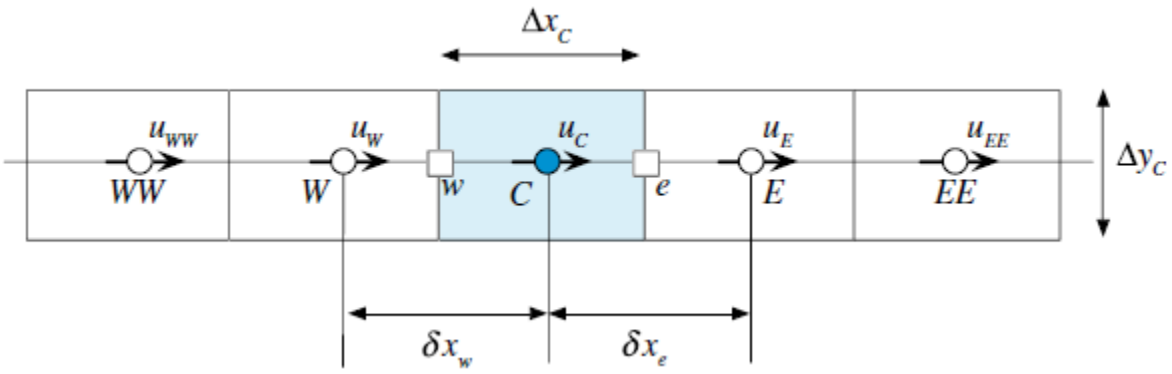

Figure 2. 1. Discretized one-dimensional flow field (Moukalled et al., 2016)

Appling the Gaussian theorem – the summation of fluxes in the control volume to mass and momentum conservation results,

$$\dot{m}_e u_e + \dot{m}_w u_w - \mu\left[\left(\frac{\partial u}{\partial x}\Delta y\right)_e - \left(\frac{\partial u}{\partial x}\Delta y\right)_w\right] = -\int_{V_c} \frac{\partial p}{\partial x} dV \tag{2.18}$$

where $\dot{m}$=mass flow rate

Depend on the flow characteristic, pressure or density-based solvers are adopted and typically, pressure-based solver is employed for incompressible flow since it has constant density. The pressure term from the Equation 2.18 can be discretized by using a central difference scheme or Gaussian theorem and it become

$$\int_{V_c} \frac{\partial P}{\partial x} dV = \int_{\partial V_c} p dy \tag{2.19}$$

$$\int_{V_c} \frac{\partial P}{\partial x} dV = \left[\frac{1}{2}(p_E + p_C) - \frac{1}{2}(p_C + p_W)\right]\frac{V_C}{\Delta x} = \frac{p_E - p_W}{2\Delta x} V_C \tag{2.20}$$

With these discretized equations, control volumes of each cell are expressed in the matrix. The size of the matrix and interacting between elements are determined by the grid.

2.5 ANSYS FLUENT 19.1 Solver

Direct solvers like Gaussian Elimination method sometimes used to solve linear algebraic equation but it requires lot of computing ability. Instead, an implicit and iterative solver is employed in Fluent 19.1 which approximates and substitutes roots while reduce residuals. The matrix for set of discretized equations is (Moukalled et al., 2016)

$$\begin{bmatrix} F & b^T \\ b & 0 \end{bmatrix} \begin{Bmatrix} u \\ P \end{Bmatrix} = \begin{Bmatrix} f_b \\ 0 \end{Bmatrix} \tag{2.21}$$

where f_b = body force and b= decomposed matrix of sources

The basic algorithm like SIMPLE Semi Implicit Method for Pressure Linked Equations) scheme rearrange the matrix (eq. 2.21) to separate in momentum and pressure terms and solve sequentially until satisfy conservation laws with velocity and pressure corrections.

$$\begin{bmatrix} F & 0 \\ B & -BD^{-1}B^T \end{bmatrix} \begin{Bmatrix} u^* \\ P^* \end{Bmatrix} = \begin{Bmatrix} f_b \\ 0 \end{Bmatrix} \quad (2.22)$$

The intermediate values are expressed with stars (*) and inverse diagonal of the force (D) is used for the approximations.

The Coupled Algorithm employs implicit method but with different approaches, which solve momentum and pressure terms simultaneously (Ansys User Guidebook). It gives more robust and precise results than the SIMPLE method, and effective for low quality meshes in transient flow analysis. The second order scheme was used for the pressure interpolation with coupled method in this analysis, which calculates pressure terms with a central differencing instead of linear or gradient interpolations. Double precision option - increases storages of each binary number used in the calculation, was utilized to increase accuracy of the analysis.

Chapter 3 Model Setup

Canal and turbine geometries were introduced in section 3.1 with brief explanation of an open channel flow characteristics. Boundary conditions for computational model are described in section 3.2. Section 3.3 presents the created model meshes used for the analysis and a grid independence study is given in 3.4.

3.1 Geometry and Canal Modeling

Naturally a canal has free surface (Figure 3.1), an interface between water and air. In an open channel setting, a fluid is subjected to different amount of shear stress according to its location. Near the walls of the channel, friction (and thus shear stress) between the moving water and the walls is high, whereas the water and air interface cause little shear stress on the moving water.

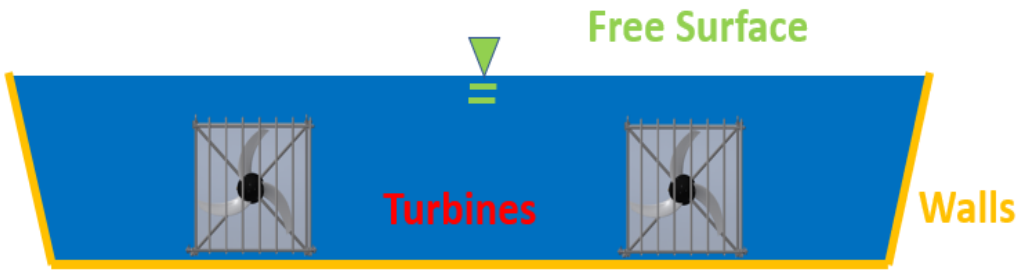

Figure 3. 1. Possible schematics of a canal and flow boundary with installation of smart turbines

When a fluid flows over a surface, acting shear stress on the liquid generates a u-velocity profile in y-direction and forms a boundary layer (Figure 3.2). The velocity profiles on the cross-sectional area of canal are not uniform, due to the presence of the free surface and since the boundary layer also develops on the canal side walls, thus impacting the vertical velocity profile.

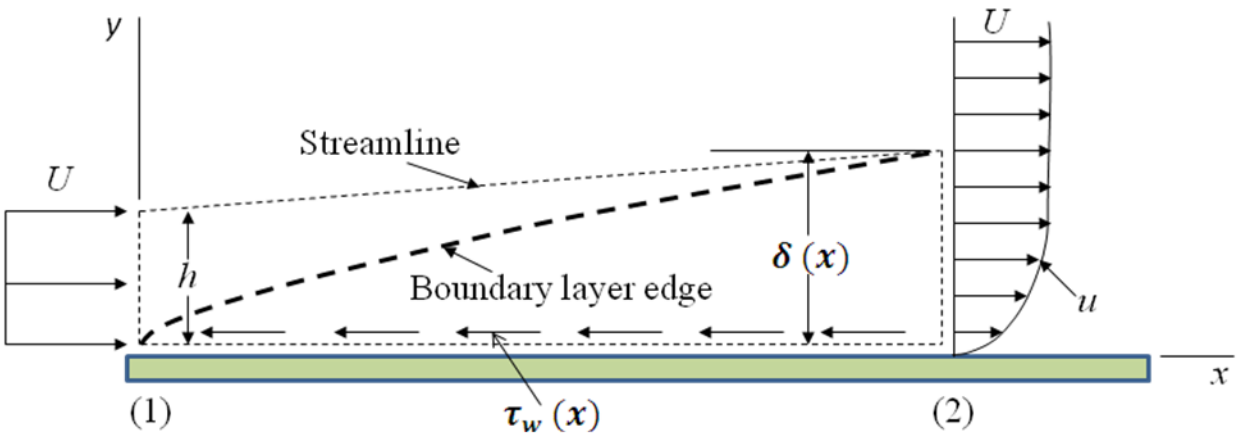

Figure 3. 2. Boundary layer formation of a flow over plane (Image from NPTEL)

Design of a canal may depend on discharge of water or surrounding geometries, and a rectangular shaped channel was used for simplifying geometry. In this problem, a flow domain is assumed as the canal and dimensions of it are shown in Figure 3.3 (a) and (b).

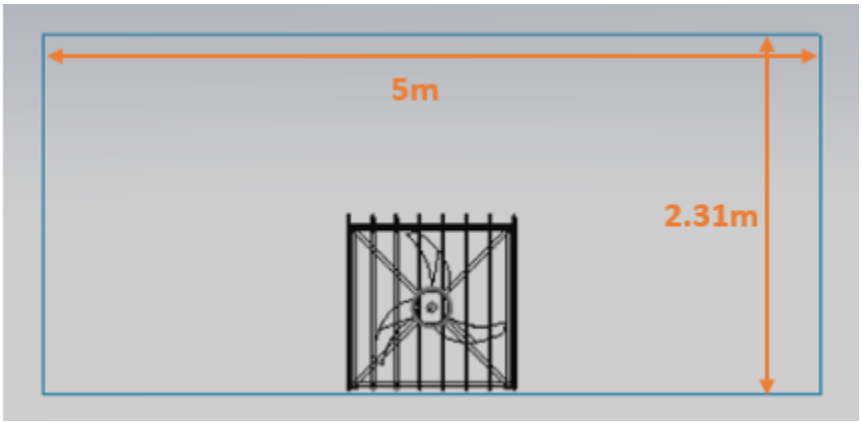

(a) Cross sectional image of the flow domain

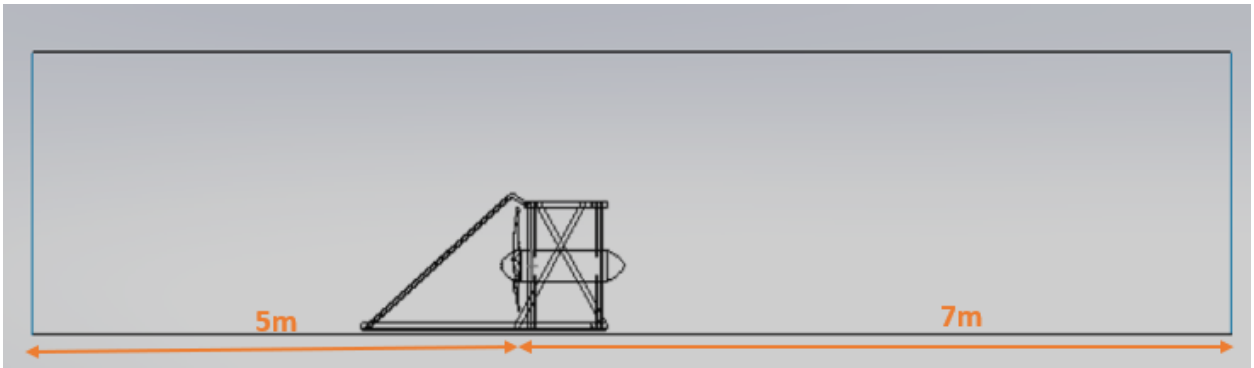

(b) Flow domain in Longitudinal direction

Figure 3. 3. Images of the flow domain with a Smart Stream Turbine

For the proper location of turbine geometry, i.e. center of the rotor, an anchor was referred from the CAD file and 2.31m of water height was used. The length between the inlet to the rotor plane was chosen as 5m, and 7m was chosen from the rotor plane to the outlet. For the flow field upstream of the turbine, no complex flow features are expected, however, the inlet section needs to be long enough for the flow to be fully developed before reaching the turbine. Further, the impact of turbine and debris protection should not extend to the domain inlet. The wake of the turbine is modeled by choosing a longer downstream simulation domain.

The blockage ratio is defined as the blocked proportional area of the domain cross-sectional area. A blockage ratio larger than zero means that the power predicted by the simulation will be higher than for the completely unblocked case. This is due to the flow being forced through the device. Often simulations are performed in very low blockage in order to minimize the effect. However, due to the confined geometry of canals the blockage ratio of the actual installation will often be quite high, so it makes sense to include this in the simulation.

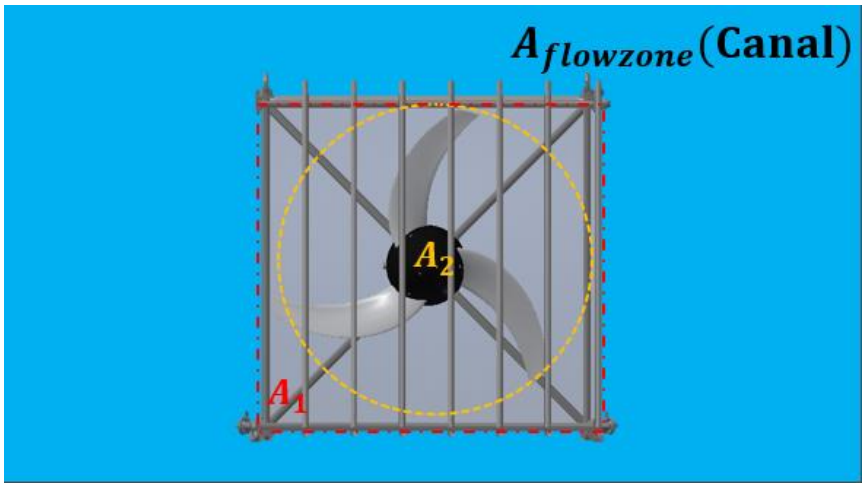

Figure 3. 4. The blocked area by the turbine: A_1 includes protector and A_2 with bare propeller

In this modeling problem, two different areas were used to calculate the blockage ratio (Figure 3.4), and the equation is shown below

$$B = \frac{A_{model}}{A_{flowzone}} \tag{3.1}$$

where B=Blockage Ratio and A=area

The frame of the turbine is assumed to have smaller effect on the flow, so blockage ratio calculated using the effective rotor area (A_2 in Figure 3.4) was used for the analysis.

As discussed in chapter 1, the Free Stream turbine was used for analysis and the turbine structure was provided from the developer, Smart Hydro Power GmbH. SOLIDWORKS 2018 has been employed to build potential canal geometries and simplify turbine structure since the assembly file provided contained all components, such as screws or bolts adding complexities on forming the mesh.

3.2 Boundary Conditions

The combined geometry of canal and turbine and its boundary conditions are shown in Figure 3.5. As discussed in section 1.3, surrounding planes of the flow domain are set as a symmetry or slip wall (zero-drag) in the most CFD analysis.

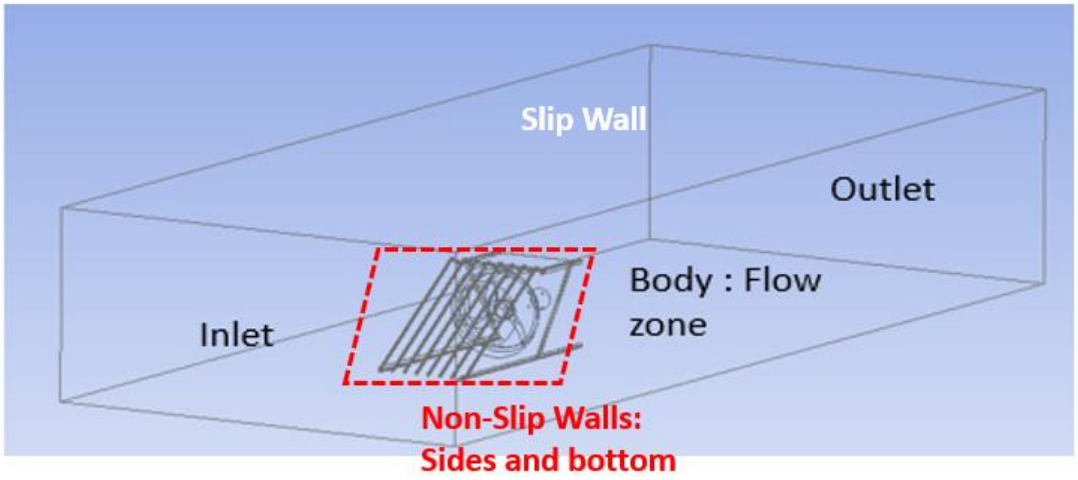

Figure 3. 5. The combined geometry used in the analysis and boundary conditions

The flow domain however, assumed as a small canal in this case featuring a free surface at the top while other planes represent canal bed and walls with friction. Typically, for an open channel flow analysis, a Volume of Fluid (VOF) method can be utilized to observe behavior of water-air interface. This method solves the continuity equation with a volume fraction of each fluid (Pokhrel, 2017), adding another level of complexity.

As has been shown, the influence of the free surface deformation on the performance of the fully submerged turbine is negligible and hence the complexity of the VOF model can be avoided by simply approximating the free surface with a slip wall (Fluent User's Guide, 2016). Therefore, the top plane is initially set as wall with slip condition (zero shear stress) due to negligible friction between air and water. For the other planes of the canal the no-slip condition was used

since shear stresses exist on the bottom and side planes. In the no-slip condition, the fluid in contact with the wall moves at the same speed as the wall and forming a boundary layer in normal direction as discussed in previous section. The same condition is applied to the turbine geometry, including blades, frame and the generator.

Inlet and outlet conditions of the canal were set as velocity inlet and pressure outlet respectively. For the velocity inlet, inflow of the fluid set as perpendicular to its cross-section, and standard temperature and pressure (1 atm, 101.3kPa) was used for outlet. A turbulent intensity I, was set as 5% based on equation 3.2,

$$I = \frac{u'}{\bar{u}} \tag{3.2}$$

Brief simulations were conducted only with a canal geometry before performing analysis with the combined geometry to observe fluid behavior in the open channel flow (Figure 3.6).

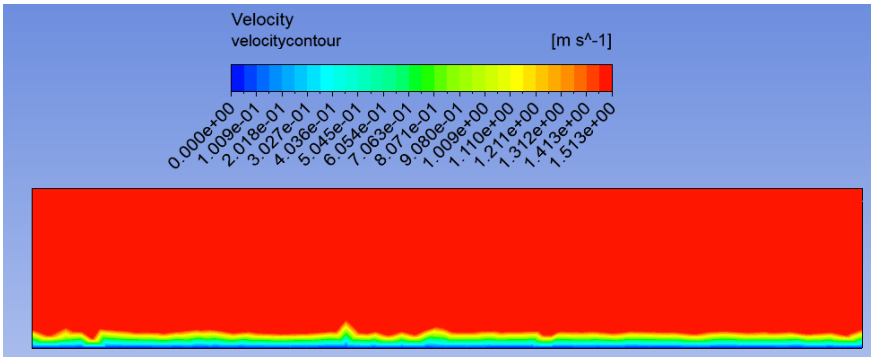

(a) Velocity profile along x-axis

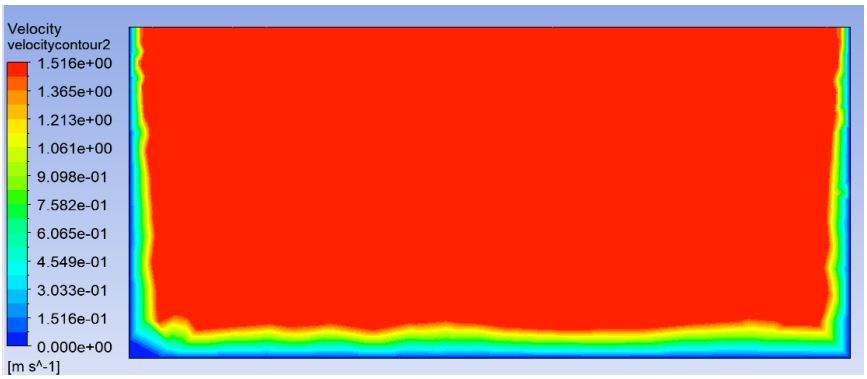

(b) Velocity profile of the cross-sectional area

Figure 3. 6. Bare canal simulation and velocity contour result

Overall, velocity of the flow became faster towards an inside and top. Drag by the wall was generally more dominant at the bottom and haven't change along the flow direction, and it agrees with characteristics of k-ω model which a development of flow is effective from the inlet.

For the turbine geometry, blades rotate with respect to its structure. Transient analysis was used since the location of blades keeps change over time. The rotating reference frame zone (Figure 3.7 (a) and (b)) had generated for mimic the rotational movement of the blades and it interact with outer mesh at each iteration.

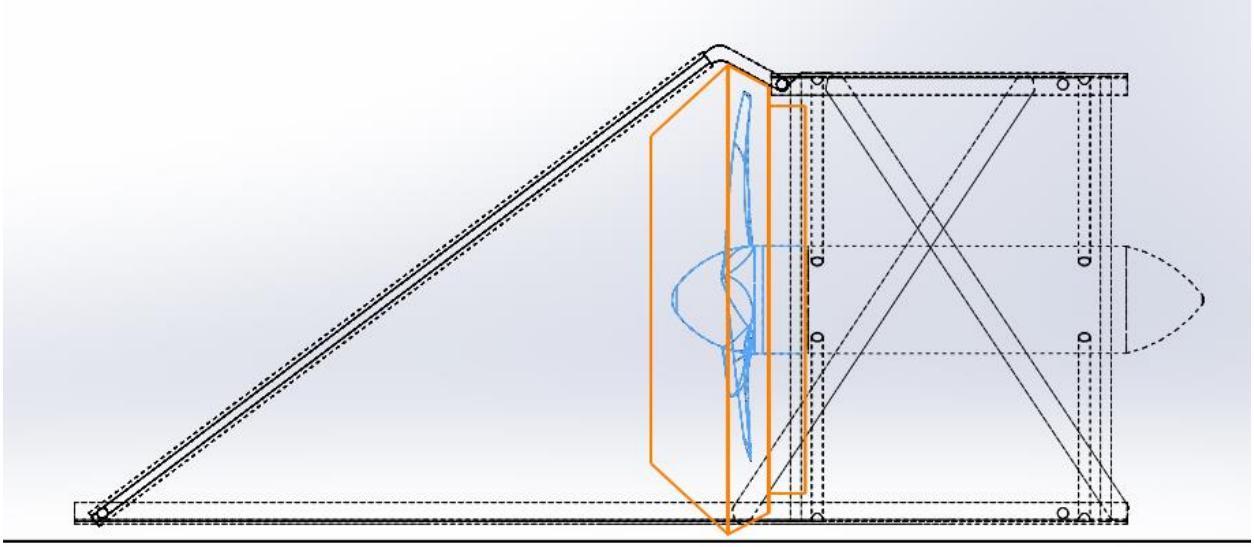

(a) Side view of the hub geometry

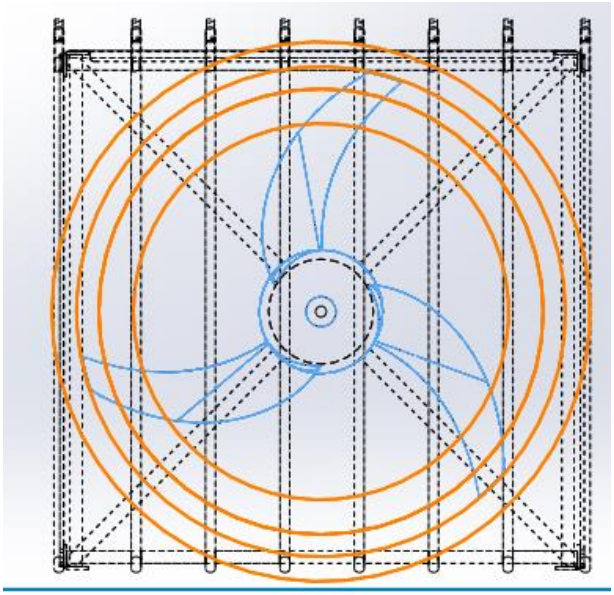

(b) Front view of the hub geometry

Figure 3. 7. The rotating reference frame which encloses the rotor is displayed with orange color

The reference frames were generated while considering geometry of the turbine frames and it enclose overall blade geometry, then set as to have same rotational speed with the blades.

3.3 Mesh Generation and Quality

Default mesh generator from fluent 19.1 have been used for mesh generations. In case of flow is turbulent, near wall function should be considered since turbulent models take account of layers (viscous or buffer) in its calculation. As discussed in section 2.2, empirical methods are employed for turbulent closures, and the first mesh size from wall is important because each model uses different size of grids to determine energy dissipation, induced by turbulence.

To calculate proper size of cells from the wall, a non-dimensional parameter of y+ (y plus) is commonly used and it defined as

$$y^+ = \frac{\rho u_\tau D_h}{\mu} \tag{3.3}$$

where u_τ= shear velocity

Density and viscosity are known parameters from material property, but to estimate shear velocity, shear stress calculation should be preceded, and it can be approximately assumed by a skin friction coefficient.

$$\tau_w = \frac{1}{2}\rho C_f u_\infty^2 \tag{3.4}$$

where C_f= skin friction coefficient, u_∞= free stream velocity, and τ_w= wall shear stress

The skin friction coefficient is function of the Reynolds number, and for the external flow it has value of

$$C_f = 0.058Re^{-0.2} \tag{3.5}$$

With these calculations, size of mesh in hub (zone 1) was decided as 0.004 m while comparably coarse cells were used on the outside of the hub (zone 2) as shown in Figure 3.8.

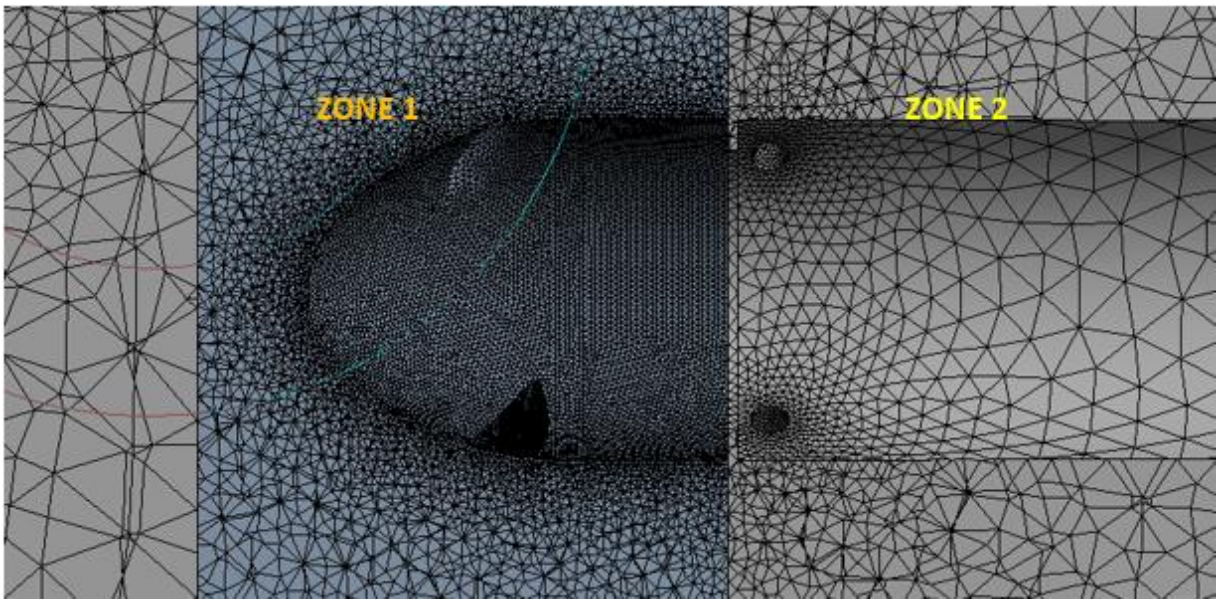

Figure 3. 8. Zone 1: Rotating reference frame, Zone 2: Stationary regions

During mesh generation, it was individually generated for each zone in the program. Images of the final mesh which have been used for physical analysis are displayed in Figure 3.9. Unstructured mesh was applied to both of fluid volumes with different size.

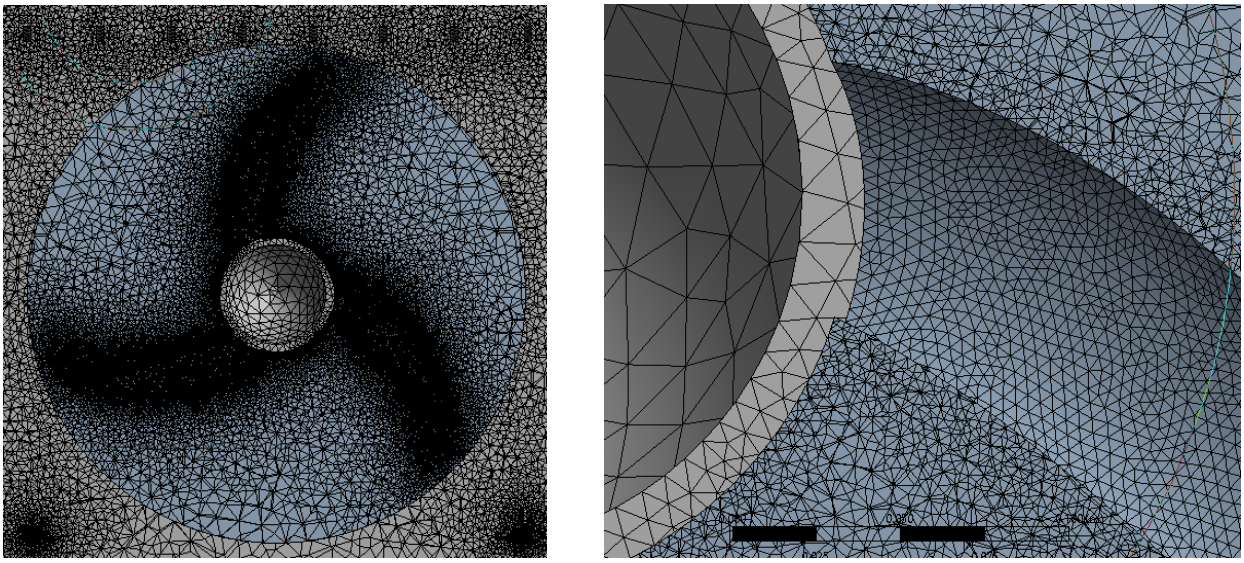

(a) Front view of generated mesh (b) Mesh near the blade

Figure 3. 9. Mesh configurations

Specifically, following controls and minimum sizes were used for mesh generation (Table 3.1)

Table 3.1 Size control and transition rate

Location	Size (m)	Transition Rate
Global	0.4	1.17
Zone 1 (Hub)	0.004	1.12
Top	0.1	1.14
Bottom	0.08	1.15
Others (Density regions)	0.08-0.1	N/A

After mesh generation, final mesh has size of

- No. of Elements: 14,640,062
- No. of Nodes: 2,580,198

Since top plane have free surface, a convergence of continuity was issued when conducting calculations. A distance between bottom wall and turbine geometry is much closer than walls on the sides while subjected to the drag force by the fluid. Therefore, transition rates of top and bottom plane were set smaller than other places to avoid these issues.

Cornell Fluent Learning Module was referred to determine quality of mesh. Orthogonal quality and skewness were investigated, and results are stated at table 3.2.

Table 3.2. Average and minimum qualities of mesh

Types	Averaged Quality	Minimum Quality
Skewness	0.21657	0.99956
Orthogonal Quality	0.78213	0.00043

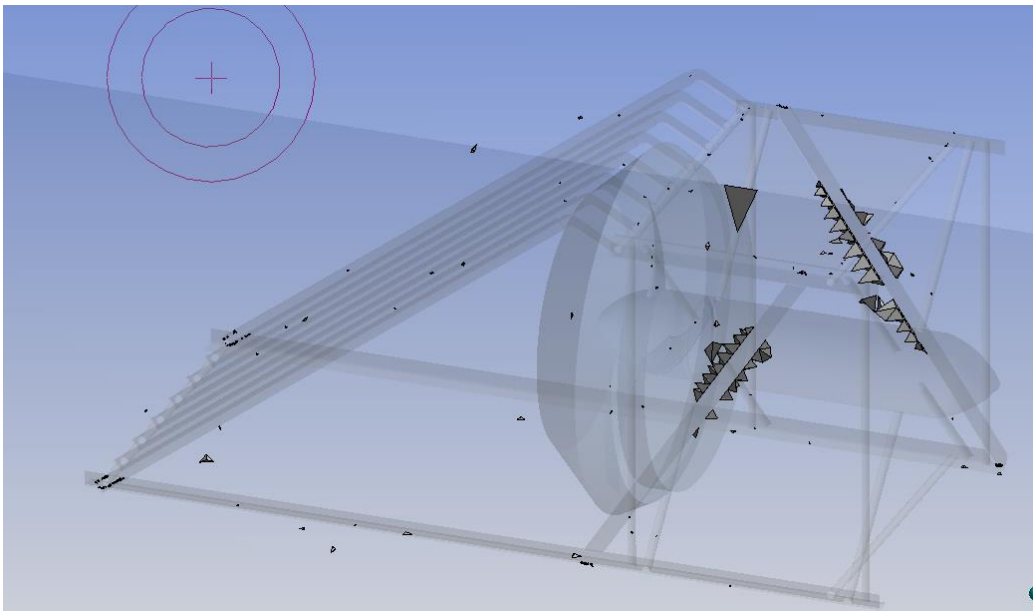

Figure 3. 10. Cells with skewness over 0.85

According to the learning module, it is desirable to have less than 0.95 of skewness and more than 0.15 of orthogonal quality to perform the analysis properly. Poor-quality cells were mostly generated near polygonal frames (Figure 3.10), and minimum qualities of the cells were less than criteria. However, these cells were ignored since the frame affect less on the flow than blade or hub zone and reduce time for calculations.

3.4 Grid Convergence Study

The results of CFD modeling is highly dependent on quality and composition of the mesh. Usually, more precise results can be achieved with higher resolution of mesh, but it consumes more computing resources.

Meshes with 7.9 7.9 to 26.7 million cell sizes had been tested. The overview of smallest and largest size of meshes are displayed in Figure 3.11 (a) and (b).

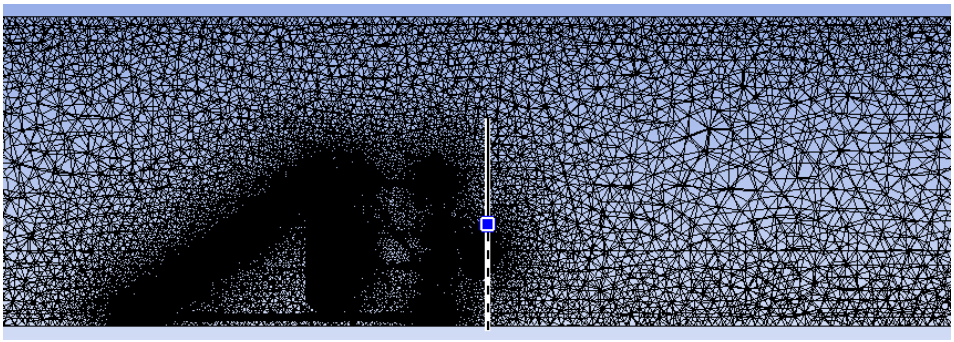

(a) Frame view of fine mesh with 26.7 million cells

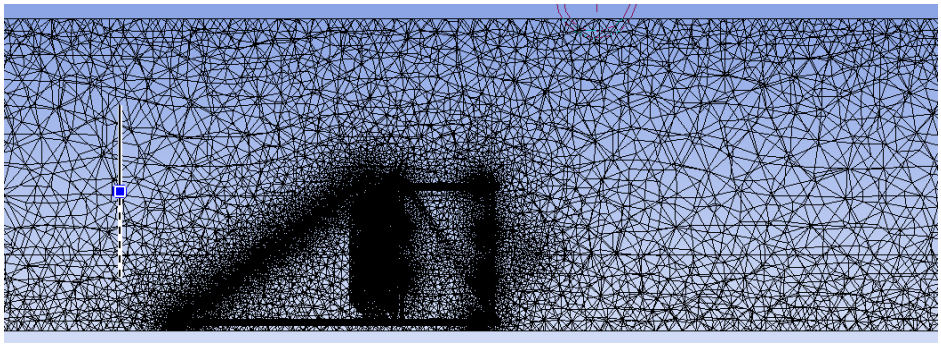

(b) Frame view of coarse mesh with 7.9 million cells

Figure 3. 11. Meshes without regional controls

With previously mentioned boundary conditions, torque obtained from blades was mainly used for the convergence study (Detailed physical conditions are stated in the next chapter). It changed with time and decreased until about 3 seconds for all cases as shown in following Figure 3.12, which agree with length of inlet to turbine geometry with stream velocity. After that, it converged at some consistent values which ranged around 42-43 Nm.

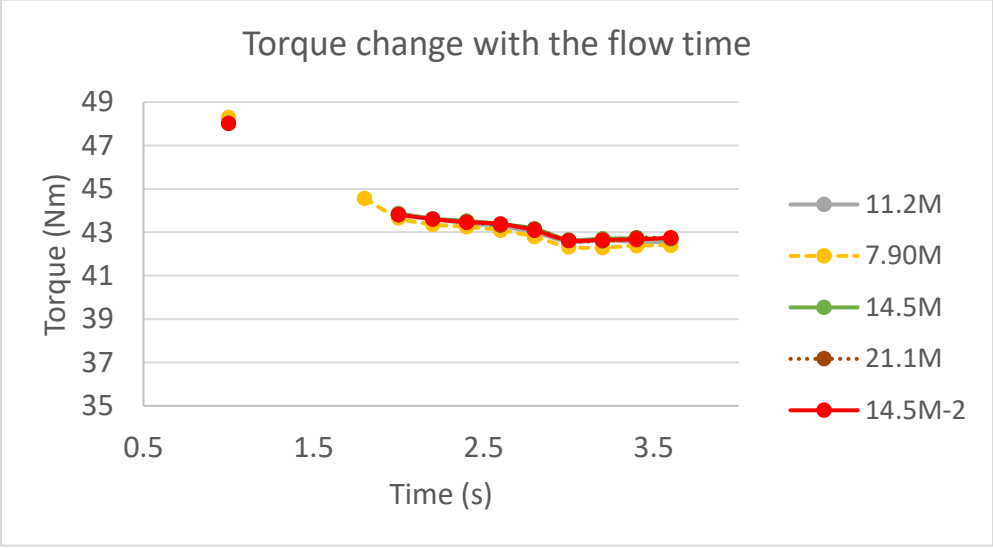

Figure 3. 12. During the transient analysis, result torque was changed over time. 14.5-2 indicates a result with regional controls

Torque was generally decreased with smaller size of meshes with same mesh controls. Increasing accuracy of the CFD could be achieved by adding controls on certain regions while maintaining coarse mesh on far places, i.e. near blades or downstream of the turbine since not much changes were observed from inlet to at the beginning of the turbine.

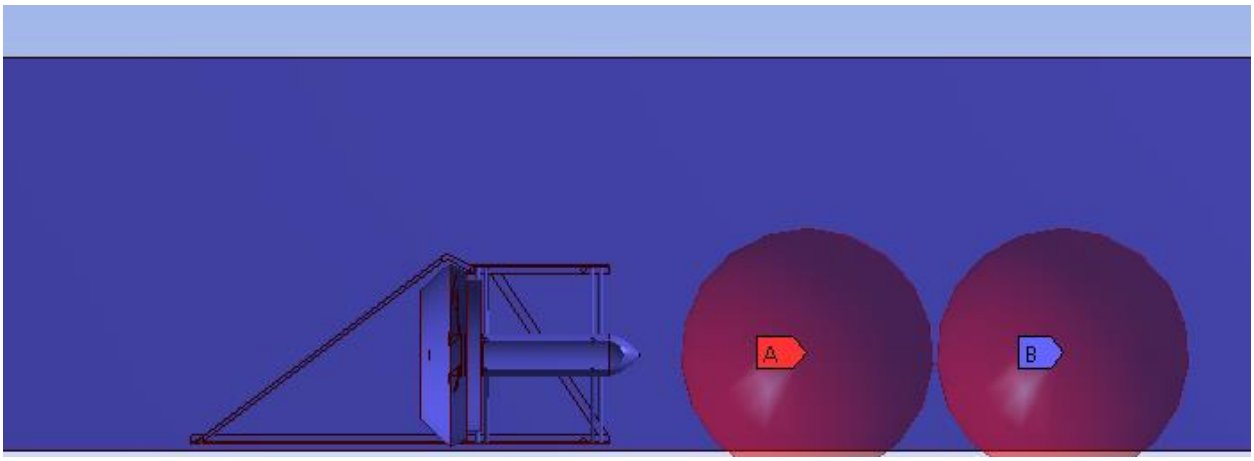

Figure 3. 13. Applied density controls over the flow domains

Therefore, two spherical density regions were finally applied as shown in Figure 3.13. Each sphere has 0.75m of radius, and detailed specifics are shown in the Table 3.3.

Table 3.3 Size and locations of regional controls

	Sphere A	Sphere B
Element size (m)	0.08	0.1
Coordinate (m)	2,0,0	3.5,0,0

Torque results at 3.4 second with different size of meshes are shown in Figure 3.14

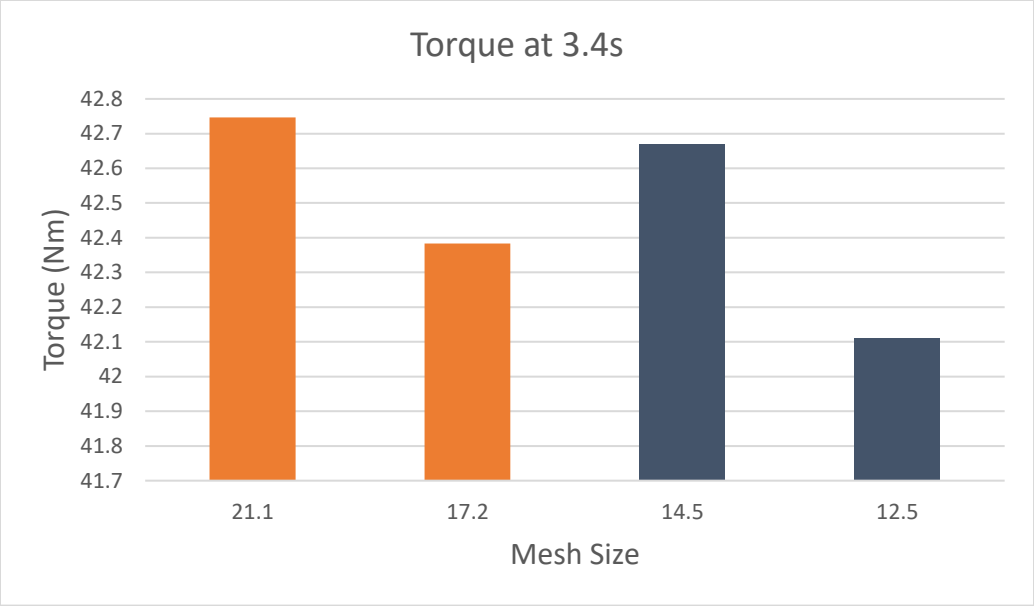

Figure 3. 14. Torque results: density control applied for 12.5 and 14.5 (previously 14.5-2 in Figure 3.12)

When 21.1 and 17.2 million elements size of meshes were made, only size and transition rate were adjusted while density controls of Figure 3.13 had applied for meshes with 12.5 and 14.5 million cells.

Table 3.4. Measured torque at 3.4 seconds of flow time with different size of meshes

Size of Mesh (Million)	Torque (Nm)	% Mesh diff	% Torq diff
21.1	42.7469		
17.2	42.3832	18.48341	1.723697
14.5	42.6699	31.27962	0.364929
12.5	42.112	40.75829	3.009005

As shown in table 3.4, torque value at 3.4 seconds with 14.5 million mesh showed much closer results with 21.1 million one than bigger sized mesh (17.2 million), which has only 0.365% of torque difference. The 12.5 million cell sized mesh could reduce time for simulations further, but

it is presumably assumed that the flow domain might not be predicted accurately, and consequently, the mesh with 14.5 million elements were used for further physical condition tests.

Chapter 4 Performance Study of the Free-Stream Turbine

Conducting calculations for the mesh, approximately with 14.5 million cells in double precision requires large computing powers. Resources from Ohio Supercomputer Center (OSC) had been used for reducing calculation times. Owens Cluster system, which have Intel Xeon E5-2680 v4 as processors had been used and it took about 22 hours to perform a single simulation when two nodes with 52 threads were used in parallel. As discussed in the section 2.5, ANSYS Fluent 19.1 had been used as the fluid solver program.

Section 4.1 shows physical condition setups for performance study of the turbine and fluid behavior in flow field are illustrated in section 4.2. Force and power outputs of the turbine are described in section 4.3 and efficiency analysis follows in section 4.4.

4.1 Physical Condition

A velocity of the stream and rotational speed of the blades were used as variables to test performance of the Smart Hydro Turbine in various physical conditions. Moderate range of stream velocities for canal were chosen while RPM of the turbine were adjusted to yield

maximum power outputs. As a result, 70, 100, 120, 150 and 180 rpm of rotational speeds were tested at 1.5 and 2 m/s of the streams.

Unique characteristics for CFD analysis came from the turbine structure and canal are previously introduced in section 1.2 and 3.1. Specific dimensions for the blade and frame are previously described in Table 1.1 and it is illustrated below Figure 4.1 (a) and (b).

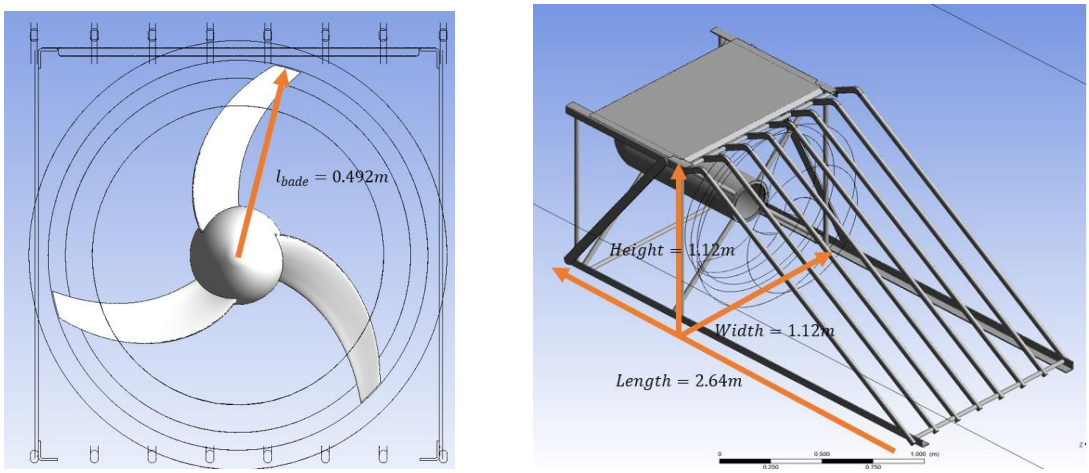

(a) Length of blade from a center of rotor (b) Frame dimensions

Figure 4. 1. Whole geometries of (a) and (b) were individually used during the post-processing

Thrust and torque of the structure were calculated based on the overall rotor and frame structures and described in following sections (4.3 – 4.4). For calculations of turbine efficiency, tip-speed ratio (λ) was used instead of angular velocity (RPM). Tip-speed ratio is useful when determining an optimal power outcome and design efficiency of air or hydrofoils. It can be calculated through tangential speeds of stream and blade tip (equation 4.1),

$$\lambda = \frac{\omega l_{blade}}{v_{stream}} \qquad (4.1)$$

where ω: angular velocity

Even with a same rotational speed, the tip speed ratio can be changed by velocity of stream, and this relationship is helpful to find ideal operating condition of the turbine in different environments.

Based on the geometries in Figure 4.1, the blockage ratio (Section 3.1: Figure 3.3 and 3.4) was calculated separately for areas covered by bare blade and includes frame structure, which resulted B_{frame} = 0.109 and B_{rotor} = 0.066. The calculated blockage ratios were used for correcting power efficiency of the turbine, originated from confined flow domain.

4.2 Flow Field Analysis

Velocity and pressure changes were investigated from front to rear parts of the turbine to see effect of the protector and rotor. A line along flow direction (x-axis) was sampled in the stream velocity of 1.5 m/s, as displayed in Figure 4.2,

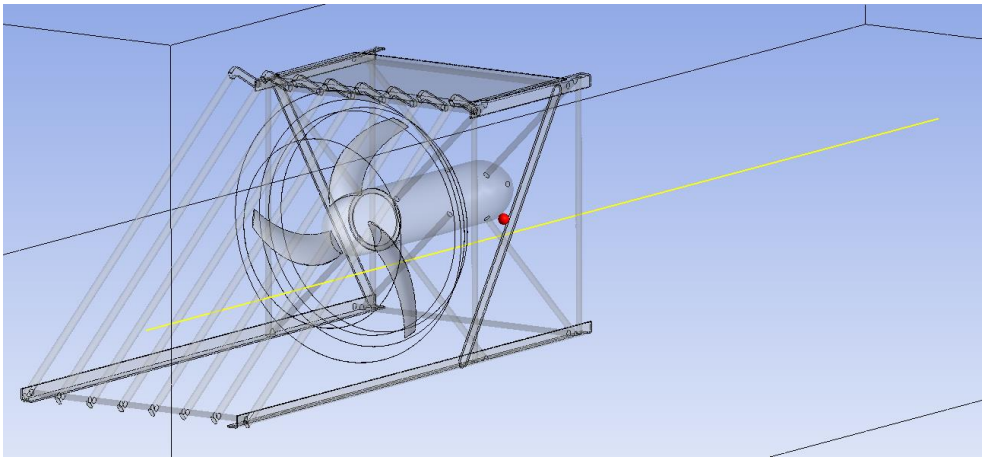

(a) Three-dimensional view of the sampled line

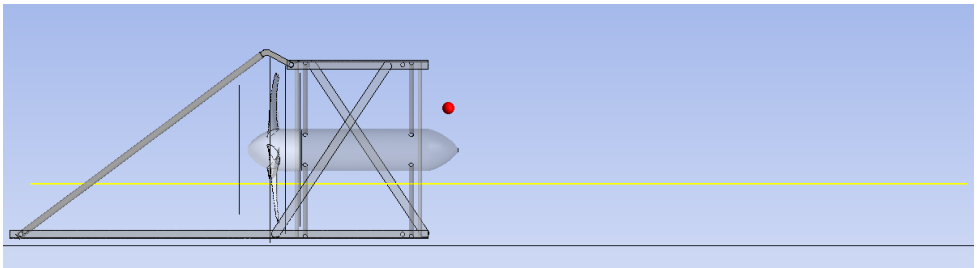

(b) Sampled line along x-direction

Figure 4. 2. Total 31 points were sampled on line located 0.2m from center of the rotor

Pressure and velocity change along x-axis are displayed in Figure 4.3 (a) and (b),

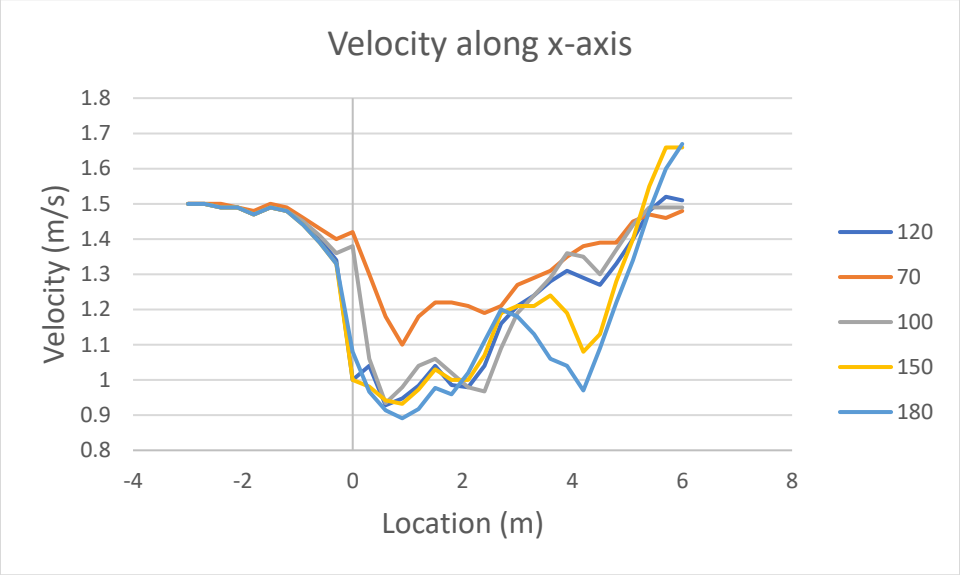

(a) Velocity (in stn frame) profile along x axis from 70-180

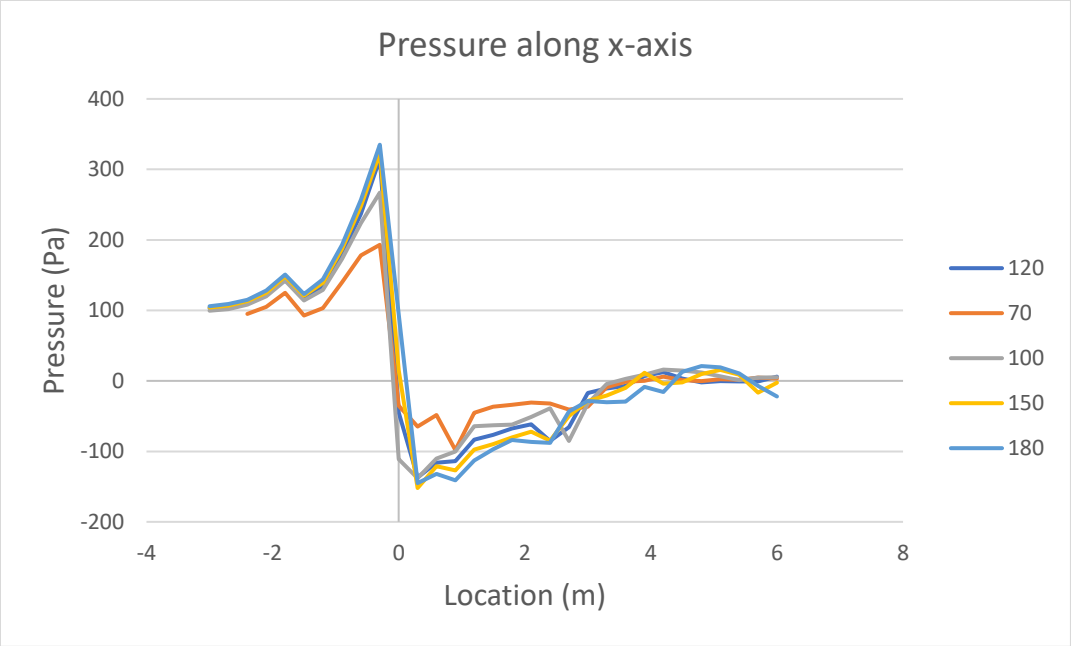

(b) Pressure profile along x axis from 70-180 rpm

Figure 4. 3. Velocity and Pressure change at 3.4 seconds of flow time

A ramp is observed in pressure and velocity profile and it agrees with frame location. Compare to a pressure drag by the blade, the ramp was not significant in both conditions. Higher rpm made a larger peak to peak amplitude of pressure and velocity before and after the blade structure location, but the changes were not significant after 120 rpm.

4.3 Torque (Thrust) analysis

Torque was numerically evaluated through a function calculator in Ansys CFD Post. Overall propeller geometry was used (Figure 4.1, (a)) when achieving data, and the testing

conditions were described in the previous Section 4.1. The results are shown in Table 4.1 and Figure 4.4.

Table 4.1. (a) Tip speed ratio and torque in the slower stream environment

1.5 m/s of stream velocity					
RPM	**70**	**100**	**120**	**150**	**180**
λ (TSR)	2.404	3.435	4.122	5.152	6.183
Torque (Nm)	57.533	51.044	42.670	30.453	16.970

(b) Tip speed ratio and torque in the faster stream environment

2.0 m/s of stream velocity					
RPM	**70**	**100**	**120**	**150**	**180**
λ (TSR)	1.803	2.576	3.091	3.864	4.637
Torque (Nm)	75.982	104.52	98.898	81.856	65.1252

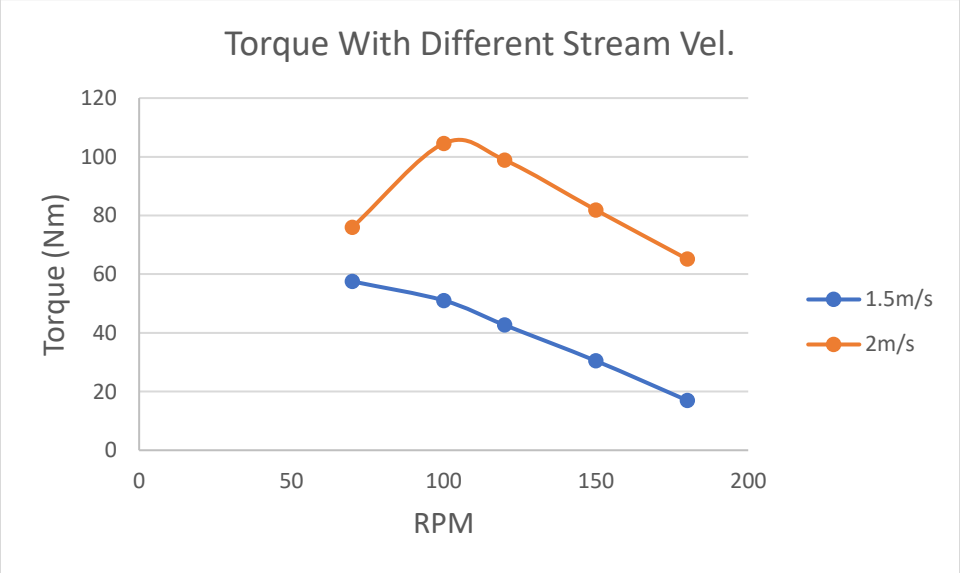

Figure 4. 4. Torque distribution (at the flow time of 3.4 sec)

Torque generally shows curved distribution and the maximum torque are observed around 100 rpm when stream has 2m/s of velocity. Lower angular velocity may necessary to find the maximum torque output when 1.5 m/s of stream, but it was skipped since higher power were yielded from the tested RPM range.

4.4 Efficiency analysis

Power outputs of motor and generator are dependent on an intensity of current or magnetic field in its system. In the generator analysis, the current is proportional to rotational velocity, therefore maximum power output can be diverse with different sets of RPM, induced by controlling intensity of magnetic flux.

Generated power from the turbine follows below relationship,

$$P = T\omega \tag{4.2}$$

where T=Torque (Nm) and P=Power (W)

After torque were investigated with various RPMs and stream velocity in the simulation, power was calculated with previous numerical results (Table 4.2 (a) and (b)) to compare analytical solutions and get power coefficients of the turbine,

Table 4.2 (a) Power outputs in the slower stream environment

1.5 m/s of stream velocity					
RPM	**70**	**100**	**120**	**150**	**180**
λ (TSR)	2.404	3.435	4.122	5.152	6.183
Power (W)	421.72	534.53	536.19	478.35	319.88

(b) Power outputs in the faster stream environment

2.0 m/s of stream velocity					
RPM	**70**	**100**	**120**	**150**	**180**
λ (TSR)	1.803	2.576	3.091	3.864	4.637
Power (W)	556.95	1094.51	1242.75	1285.79	1227.61

and below Figure 4.5 show power output with different rotational velocities,

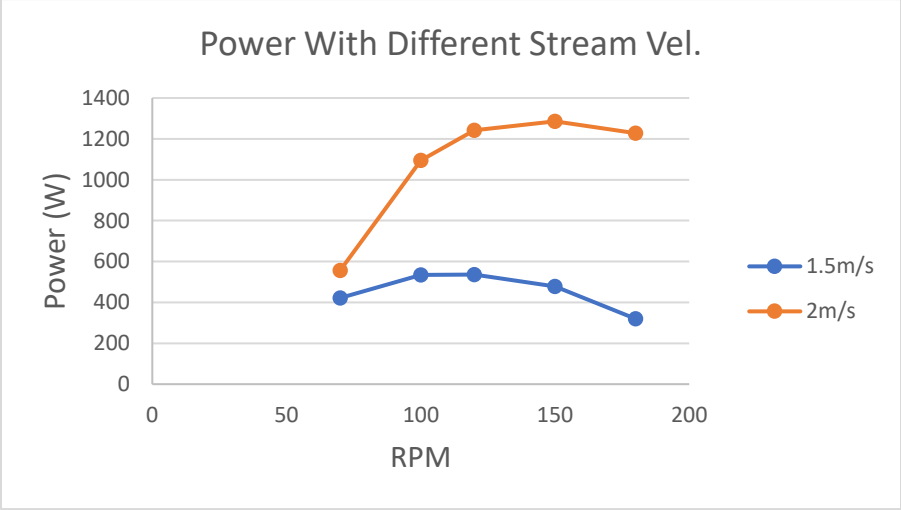

(a) Power distribution (at the flow time of 3.4 sec) with different RPM

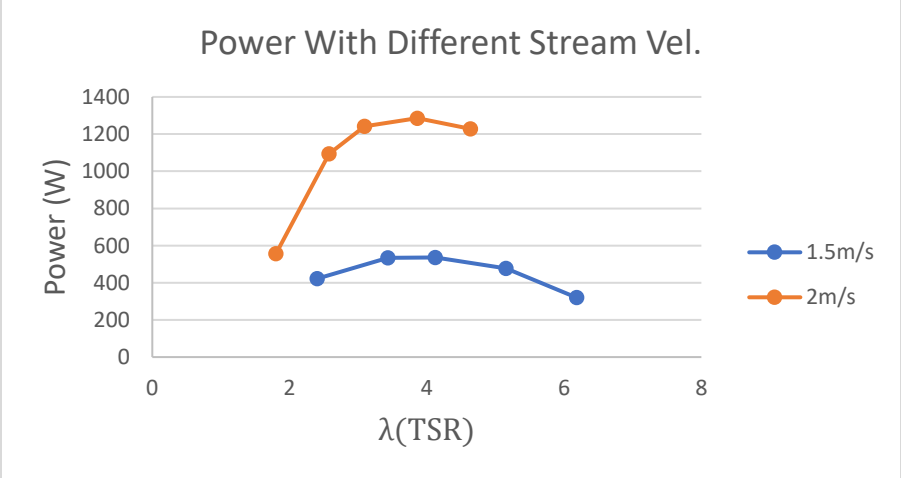

(b) Power distribution (at the flow time of 3.4 sec) with various RPM

Figure 4. 5. Measured power from simulation results at 1.5 and 2m/s of stream velocity

Power outputs of the turbine showed a peak near 100 to 120 rpm for 1.5 m/s of stream speed and around 150 rpm for 2m/s of the stream. Both results showed maximum outcomes approximately at 3.8 of the tip speed ratios.

Available power from the axial flow by a rotor can be derived from the Bernoulli equation, and it eventually is expressed as,

$$P_{in} = \frac{1}{2}\rho A V^3 \quad (4.3)$$

where P_{in}=Available maximum power

From this equation, the maximum power output in STP condition should be 1281 W for stream velocity of 1.5m/s and 3036 W for 2.0m/s of flow.

A power coefficient of an axial turbine can be calculated through investigate the ratio of overall power inputs from the stream or flow to actual power output from the turbine,

$$C_p = \frac{P_{out}}{P_{in}} \quad (4.4)$$

where C_p= Power Coefficient

Power coefficient at stream velocity of 1.5 and 2.0 m/s with different rotational velocity are described in table 4.3 (a) and (b).

Table 4.3 (a) Power coefficients in the slower stream environment

1.5 m/s of stream velocity					
RPM	**70**	**100**	**120**	**150**	**180**
λ (TSR)	2.404	3.435	4.122	5.152	6.183
Power (W)	421.72	534.53	536.19	478.35	319.88
C_p	0.3292	0.4173	0.4186	0.3734	0.3059

(b) Power coefficients in the faster stream environment

2.0 m/s of stream velocity					
RPM	**70**	**100**	**120**	**150**	**180**
λ (TSR)	1.803	2.576	3.091	3.864	4.637
Power (W)	556.95	1094.51	1242.75	1285.79	1227.61
C_p	0.1834	0.3605	0.4093	0.4235	0.4043

Below Figure 4.6 illustrates power coefficient changes with different tip speed ratio in different stream speeds,

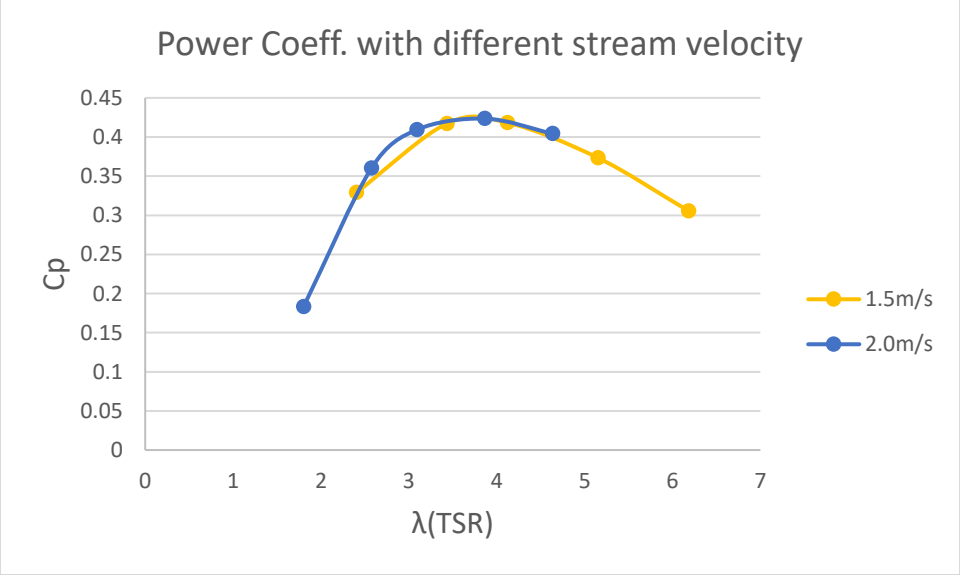

Figure 4. 6. Power coefficient distribution (at the flow time of 3.4 sec)

As shown in Figure 4.6, power coefficient curves with different speed generally coincide. Compare to maximum efficiency of an axial turbine, known as Betz Limits: (C_p=59%) the results showed less than something value and it may indicate there's some room for improvements of hydrofoil design to extract more power.

4.5 Blockage ratio correction factors

As previously discussed in section 3.1 and 4.1, the blockage ratio has importance when predict performance of turbines accurately, since an acceleration of flow triggered by the turbine structures and boundaries of canal to limited flow domain may be deemed significant. Since the blockage ratio is smaller than 1, the maximum power coefficient is proportional to its squared value (Garrett and Cummins, 2017),

$$C_{P,max} \propto \frac{1}{(1-B^2)} \tag{4.5}$$

From this relationship, increments of the turbine performance by the flow domain were estimated as 1.2% and 0.44% with the blockage ratios used in this research, B_{frame} = 0.109 and B_{rotor} = 0.066.

Chapter 5 Conclusions

Section 5.1 and 5.2 are devoted for validations of simulation results through comparing with previous physical experiment of turbine and computational way. Shortcomings came from a numerical validation is explained in section 5.3 with possible future works.

5.1 Experimental Results

Results from CFD modelling were compared with an experimental test outcome to confirm simulation results. According to the Smart Hydro Power GmbH, the Smart Free Stream Turbine generates maximum 5000 watts when it was tested in a towing tank (Figure 5.1).

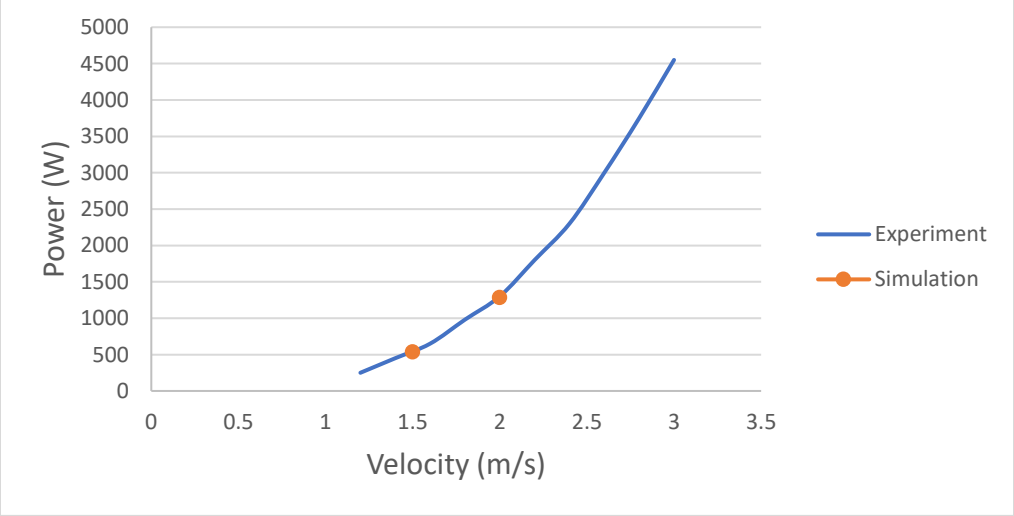

Figure 5. 1. Power outcome with different stream velocity (Captured from the homepage). Blue arrows indicate tested velocities in this study.

The maximum outputs from simulation resulted approximately 535 and 1095 Watts (Section 4.4) and it is well agreed with experimental results.

The towing tank has a cross-sectional area of 4x8 m^2, and the maximum power performance also affected by geometrical limitations. The blockage ratio correction factor is also applicable to this physical test results and the blockage ratio resulted as B_{frame}'=0.0392 and B_{rotor}'=0.0238 from the size of the tank and turbine structure. With these obtained blockage ratios, the maximum generated power from physical test was increased by 0.154% and 0.567% with the relationship of Equation 4.5. From this, the power output difference between simulations and tests would be increase due to the larger blockage were used during the modeling but the effect could be very small since the biggest change of output assumed about 1%.

5.2 Numerical validations

Although simulation results well agree with experimental results, the simulation results showed lack of precision with a numerical validation method of Y+ (Section 3.3). Size of grid is important to capture shear effects, which originated from walls with friction. In case of k-ω SST model is employed, the ideal Y+ should be less than 1 and around 11 for standard model.

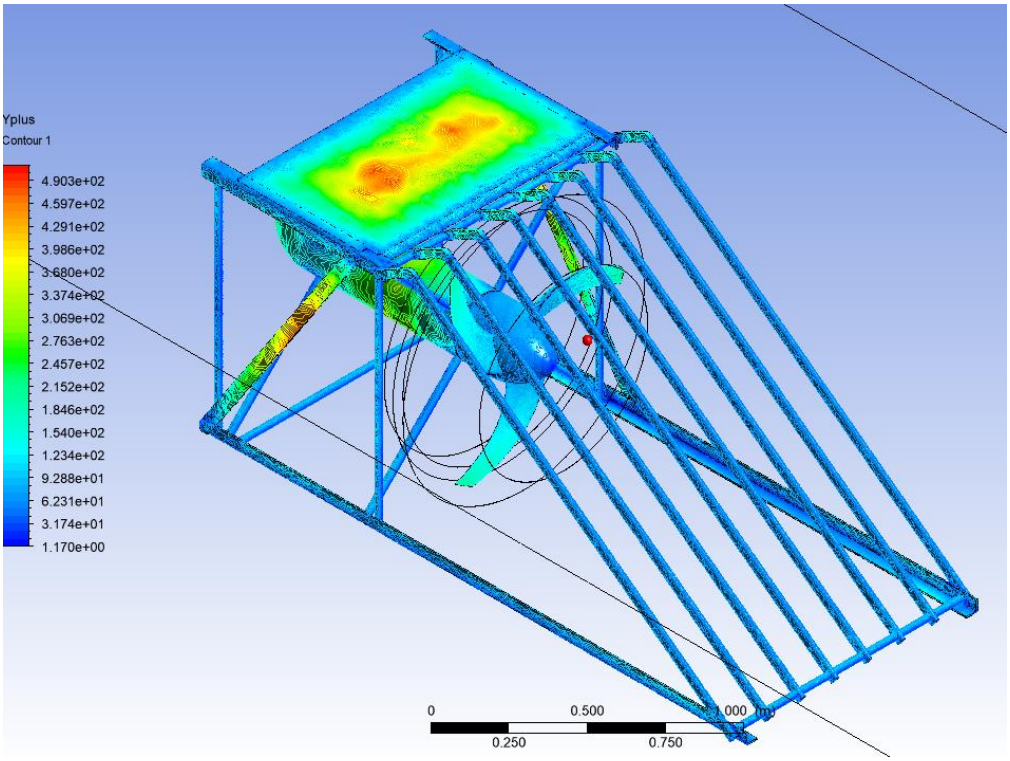

Figure 5. 2. Y+ results at the rotor and protector structure

However, the Y+ resulted over a 100 at the tip and rear side of the blade and few parts of frames had the value around 500. The structure may not necessarily have desired Y+ value since effect is small but grids near the rotor should be reduced to get proper data. A hydrokinetic turbine research was performed with Y+ over 10 with the SST model (Riglin et al, 2016) and showed close results with experimental data, it is possible to predict power outcome inaccurately in this study. Even though the turbine structure includes geometry of the generator, the simulation method used in this study solely regarding hydrodynamics without loss from the system. Many CFD analysis of turbines show out-performed results and the residual energy considered as the loss. In this study, it seems the loss from the system coincides with less turbulence energy

dissipations due to large girds. Incorrect assumption of the Y+ at the beginning of the research originated from using the stream velocity as function of it, not changing speed near rotor blades.

Mass flow rates at the inlet and outlet were also investigated to see if there are any unexpected behaviors of the fluid in flow regime and confirm convergence of the continuity during calculations. At the invested flow time of 3.4 seconds, it changes only with different stream velocity while rpm doesn't affect the results (Table 5.1).

Table 5.1. Mass flow rate (kg/s) at the inlet and outlet

Stream Velocity(m/s)	Boundary Condition	RPM		
		70	150	180
1.5	Inlet	17225.7	17225.7	17225.7
	Outlet	-17225.9	-17225.9	-17225.9
2	Inlet	22967.6	22967.6	22967.6
	Outlet	-22967.9	-22967.9	-22967.9

The mass flow differences between inlet and outlet were around 0.001% for both cases and it indicates the backflow or adverse pressure gradients are not appeared in the flow domain.

5.3 Future works

A mesh generator used during the research, which provides a function of importing external geometry sources supports several options for regional refinements, but the algorithm used for meshing seemed not robust enough for very complex geometry, such as the turbine structure used in the study. Applying inflation layer had been limited due to convergence issues,

therefore torque extracted from blade geometry may not accurately capture all the energy generated from the rotor without loss. Tests with refined and higher quality meshes is preferred to further validation. Also, employing multiple turbines or complex canal geometry maybe helpful to anticipate actual power outcomes in real-life applications. Evaluating cost before install turbine could be possible if they keep showing consistent results.

Appendix

Since the Ohio Supercomputer Center uses Linux based system, it was necessary to write proper commend to read case and data files from Fluent 19.1.

Following commend were used to operate system

```
#PBS -N ondemand/sys/myjobs/basic_ansys_fluent_parallel
#PBS -l walltime=06:10:00
#PBS -l nodes=2:ppn=28
#PBS -j oe
#PBS -l software=ansys+1%ansyspar+52
#PBS -S /bin/bash

# A basic FLUENT Parallel Job
# Further details at:
#          https://www.osc.edu/resources/available_software/software_list/ansys/fluent

set echo on
hostname
#
# The following lines set up the FLUENT environment
#
module load ansys
#
# Move to the directory where the job was submitted from and
# create the config file for socket communication library
#
cd $PBS_O_WORKDIR
cp /users/oscgen/xwang/Fluent/Demo_tmi_fluent/test.* .
#
# Create list of nodes to launch job on
rm -f pnodes
cat  $PBS_NODEFILE | sort > pnodes
export ncpus=`cat pnodes | wc -l`
#
#   Run fluent
fluent 3ddp -t$ncpus -pinfiniband.ofed -cnf=pnodes -g < v2_100.jou
```

From the script contents, the precision was adjusted to have double precision while a journal file was used for specifying name of files, time step size and iterations.

Contents of the journal file are,

```
file/read-case v2_100-1-01120.cas
file/read-data v2_100-1-01120.dat                    ;*continuous simulation

solve/initialize/hyb-initialization                  ;*In case of initialize is necessary
solve/set/time-step                                      ;timestep size
0.0025
solve/dual-time-iterate                          ;number of timesteps
2000
10                                                                  ;iterations

exit
ok
```

Bibliography

ANSYS, Inc. (2016). *Ansys Fluent Theory Guide 17.2*. PA

ANSYS, Inc. (2016). *Ansys Fluent User's Guide 17.2*. PA

Belloni, C. (2013). 'Hydrodynamics of Ducted and Open-Centre Tidal Turbines'. DPhil thesis, *University of Oxford.*

Garrett, C. and Cummins, P. (2007). The efficiency of a turbine in a tidal channel. Journal of Fluid Mechanics, 588, 243-251.

Giorgi, S., and Ringwood, J.V. (2013). Can Tidal Current Energy Provide Base Load? (2013). *Energies* (19961073), 6(6), 2840-2858.

Ghosh, T.K., and Prelas, Mark. (2011). *Energy Resources and Systems*. Springer. Switzerland.

Kajishima, T., Taira, K., (2017). *Computational Fluid Dynamics*. Springer. Switzerland

Lachance-Barrett, S. (2018). 'Cornell Fluent Learning Module: Wind Turbine Blade FSI (Part 1)'. Retrieved from https://confluence.cornell.edu/display/SIMULATION/

Madrigal, Alexis. (2008), Nation's first underwater wind turbine installed in old man river Retrieved from https://www.wired.com/2008/12/hydrokinetic/

Moukalled, F., Mangani, L., and Darwith, M. (2016). *The Finite Volume Method in Computational Fluid Dynamics*. Springer. Switzerland.

Muratoglu, A., Yuce, M.I. (2017). Design of a River Hydrokinetic Turbine Using Optimization and CFD Simulations. *Journal of Energy Engineering*, 143(4), 1-11

NPTEL. Viscous incompressible flow. Retrieved from (2019, April 10) https://nptel.ac.in/courses/101103004/module5/lec10/1.html

Pokhrel, S., (2017). Computational Modeling of a Williams Cross Flow Turbine.

Wright State University.

Riglin, J., Carter III, F., Oblas, N., Schleicher, W. C., and Oztekin, A. (2016). Expreimental and Numerical characterization of a full-scale portable hydrokinetic turbine prototype for river applications. *Renewable Energy: An International Journal*, 99, 772-893.

Smart Hydro Power. Smart Free Stream. Retrieved from (2019, April 3) https://www.smart-hydro.de/renewable-energy-systems/

Stegman, A., de Andres, A., Jeffrey, H., Johanning, L., and Bradley, S. (2017). Exploring marine Energy Potential in the UK Using a Whole Systems Modelling Approach. *Energies* (19961073), 10(9), 1251.

Tampier, G., Troncoso, C., and Zilic, F. (2017). Numerical analysis of a diffuser-augmented hydrokinetic turbine. *Ocean Engineering*, 145, 138-147.

U.S. Energy Information Administration. Total Electric Power Industry Summary Statistics, 2017 and 2016. Retrieved from https://www.eia.gov/electricity/annual/html/